Inorganica Chimica Acta 520 (2021) 120313

Contents lists available at ScienceDirect

Inorganica Chimica Acta

journal homepage: www.elsevier.com/locate/ica

Research paper

Synthesis of $BaTiO_3$-$CoFe_2O_4$ nanocomposites using a one-pot technique

Fatima Sayed [a,*], Deep Chandra Joshi [a], Ganesh Kotnana [a], Davide Peddis [b,c], Tapati Sarkar [a,*], Roland Mathieu [a,*]

[a] Department of Materials Science and Engineering, Uppsala University, Box 35, SE-751 03 Uppsala, Sweden
[b] Dipartimento di Chimica e Chimica Industriale, Università degli Studi di Genova, Via Dodecaneso 31, Genova 16146, Italy
[c] Istituto di Struttura della Materia – CNR, Area della Ricerca di Roma1, Monterotondo Scalo, RM 00015, Italy

ARTICLE INFO

Keywords:
Nanoparticles
Nanocomposites
Magnetic
Dielectric
Oxides
Sol-gel synthesis

ABSTRACT

Low-cost and scalable sol–gel chemistry was employed to obtain ferroelectric-ferrimagnetic $BaTiO_3$-$CoFe_2O_4$ nanocomposites. In a novel one-pot synthesis method, both the constituent phases of nanocomposites are formed during the same time and symbiotically participate to each other's growth. X-ray powder diffraction evidences the phase purity of the systems, with average crystallite sizes in the order of 20 nm for the $BaTiO_3$ phase. The optimization of the synthesis conditions, precursors, and chemical agents for nanoscale $BaTiO_3$ and $BaTiO_3$-$CoFe_2O_4$ nanocomposites is presented, together with the magnetic and/or dielectric properties of the obtained materials. $BaTiO_3$-$CoFe_2O_4$ nanocomposites with up to 20% $CoFe_2O_4$ volume fractions were found to display ferrimagnetic properties at room temperature akin to those of $CoFe_2O_4$, while preserving a dielectric behavior reminiscent of $BaTiO_3$. Preliminary results describing the spin coating of $BaTiO_3$ and $BaTiO_3$-$CoFe_2O_4$ nanocomposites as thin films are also reported.

1. Introduction

There is an ever-growing number of technological applications which requires new materials with improved performance, or materials not built up of rare and/or expensive chemical elements. For example, multiferroics are considered for the next generation electronics [1], as they may e.g., display magnetoelectric effects allowing the switching of magnetic states with small electrical voltages [2]. It is thus necessary to design materials with tightly coupled magnetic and dielectric properties. A possible route toward such new materials are composite materials homogeneously combining magnetic and dielectric materials on the nanoscale (e.g. bi-phasic nanocomposites of ferroelectric $BaTiO_3$ and ferrimagnetic $CoFe_2O_4$ [3–6]). $BaTiO_3$ has a tetragonal structure and is ferroelectric at room temperature (ferroelectric Tc ~ 393 K) [7]. $CoFe_2O_4$ has an inverse spinel structure and is ferrimagnetic below ~790 K. $CoFe_2O_4$ (CFO) has a relatively large magneto-crystalline anisotropy and relatively high saturation magnetization [8] and may hence be employed as a "hard" magnetic phase in "hard/soft" bi-magnetic nanocomposites [9]. Such nanocomposites, with both large coercivity and high saturation magnetization inherited from their hard and soft constituent phases, respectively, could be used as permanent magnets [10].

A few strategies have been considered to obtain nanocomposites of transition metal oxides with strongly coupled constituent phases. Satisfactory results were obtained using preformed particles of one of the phases as "seeds" for particles of the second one, thus warranting the homogeneous dispersion of the first phase (e.g. $CoFe_2O_4$) within the matrix formed by the second one (e.g. $BiFeO_3$) [9,11]. A tight integration and magnetic coupling were evidenced in those systems [9,11].

The approach was further refined in a low-temperature sol–gel synthesis in which the particles of both phases are instead symbiotically formed at the same time; each growth participating to that of the other phase [12,13]. This "all-in-one", one-pot synthesis method, could successfully be used to obtained novel (Pb,Zr)TiO_3-$CoFe_2O_4$ [14] and $LaFeO_3$-$CoFe_2O_4$ [13] nanocomposites. Interestingly, it was shown in the latter case that the corresponding sols could be spin coated onto substrates, yielding bi-magnetic composite thin films of $LaFeO_3$-$CoFe_2O_4$ [15].

In the present article, we report the optimization of the synthesis of $BaTiO_3$ nanoparticles and $BaTiO_3$-$CoFe_2O_4$ nanocomposites using sol–gel chemistry. The nanocomposites were synthesized using a novel one-pot method involving the symbiotic growth of each constituent phase. The structural properties of the compounds are presented, and their physical (magnetic and/or dielectric) properties illustrated. The

* Corresponding authors.
E-mail addresses: fatima-sayed@hotmail.com (F. Sayed), tapati.sarkar@angstrom.uu.se (T. Sarkar), roland.mathieu@angstrom.uu.se (R. Mathieu).

https://doi.org/10.1016/j.ica.2021.120313
Received 28 December 2020; Received in revised form 17 February 2021; Accepted 21 February 2021
Available online 26 February 2021

feasibility to obtain bi-phasic thin films by spin coating is also discussed.

2. Experimental details

Chemical reactions and heat treatments were optimized to synthesize phase-pure single-phase nanoparticles of $BaTiO_3$ (BTO), as well as $BaTiO_3$-$CoFe_2O_4$ nanocomposites rather than solid solutions. Synthesis details including solvents, chelating agents, precursors, and other reactants, as well as temperatures and processes are given throughout the article. The final materials were obtained in powder form, from solutions. In some cases, the obtained solutions were spin coated on cleaned Si wafers (2 cm × 2 cm). The spinning speed was set at 3000 rpm and spinning time 30 s. The coated wafer was then baked on a hot plate at a temperature of 200 °C for 5 min. The baked dry wafers were then annealed at 650 °C for 1 h (heat ramp of ~ 6 °C/min; normal furnace cooling).

Structural analysis was performed by X-ray powder diffraction (XRPD) using a D-5000 diffractometer with CuK_α radiation operating at 40 kV and 30 mA. The data were collected in the range 2θ = 20–80°, with a step size of 0.02°. Rietveld analyses were performed using the FULLPROF suite [16].

Magnetic field-dependent magnetization of the samples was collected using a superconducting quantum interference device (SQUID) magnetometer from Quantum Design Inc. Magnetic hysteresis loops were recorded at T = 5 K and 300 K in the −/+ 5T field range. Direct current demagnetization (DCD) curves were collected at T = 5 K on the same instrument. Dielectric measurements were performed in the temperature range of 100 K–500 K and frequency range of 100 Hz–2 MHz, using an Agilent E4980 precision LCR meter and cryostat from JANIS. Polarization P - electric field E hysteresis loops were recorded at room temperature using a custom Sawyer-Tower circuit. Powder from the samples was sintered into cylindrical pellets whose sides were coated with silver paste electrodes.

3. $BaTiO_3$ nanoparticles

A solution with 0.1 M concentration was prepared by dissolving 0.00169 mol (0.4417 g) of Ba-nitrate $Ba(NO_3)_2$ (Sigma–Aldrich, ≥99%

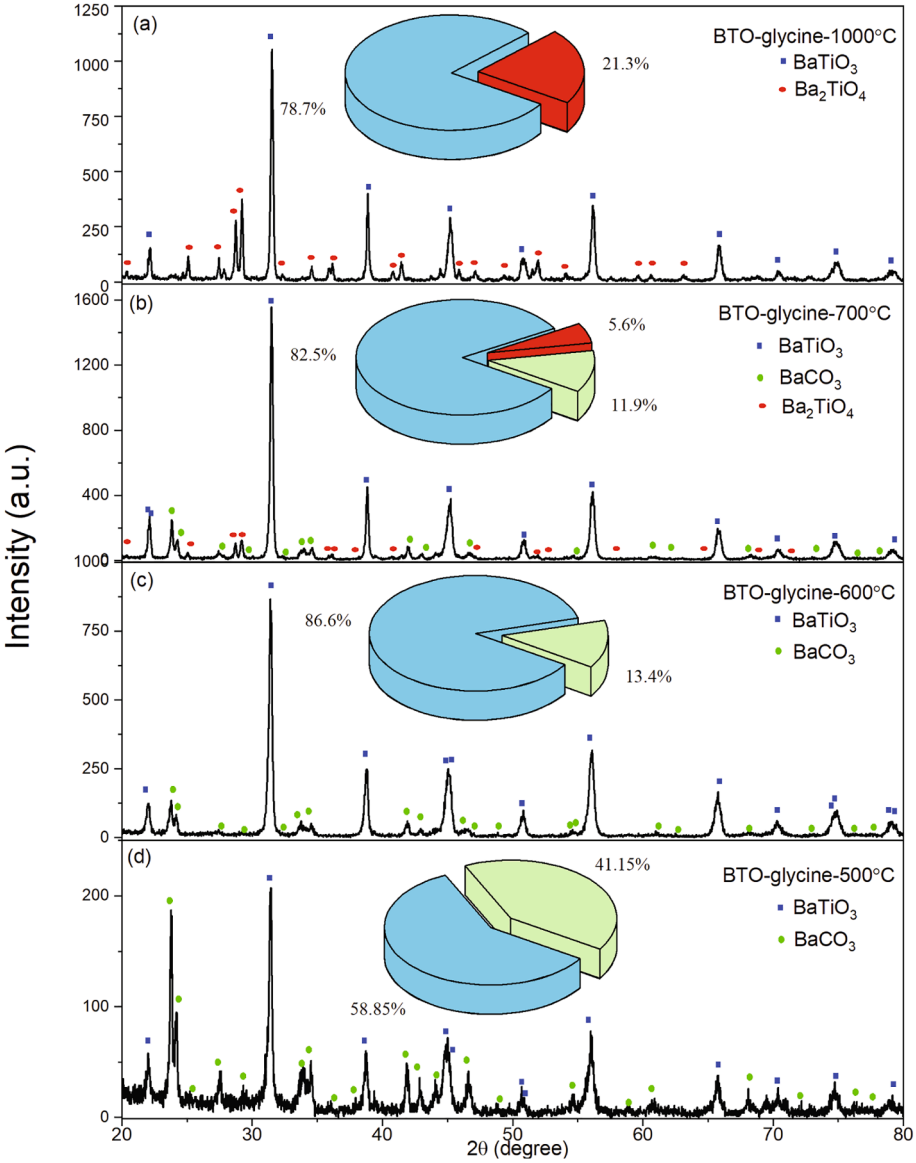

Fig. 1. XRPD patterns for BTO nanoparticle systems prepared using the glycine route, using different final annealing temperatures: (a) 1000 °C, (b) 700 °C, (c) 600 °C, and (d) 500 °C. Reflections for BTO, $BaCO_3$, and Ba_2TiO_4 are identified in the different panels. The pie-charts shown in the insets represent the quantitative phase analysis performed using the Reference Intensity Ratio (RIR) method.

purity) and 0.00169 mol (0.4803 g ≡ 0.5 ml) of Ti-isopropoxide Ti[*OCH*$(CH_3)_2]_4$ (Sigma–Aldrich, ≥97% purity) in 16.9 ml distilled water. 0.00338 mol of chelating agent (0.2537 g of glycine or 0.649 g of citric acid) were then added, together with a small amount of nitric acid (1.2 ml). The solution was stirred using a magnetic stirrer at a temperature of 80 °C for a duration of 20 min. The temperature was then increased to 150 °C and maintained until a gel formed (typically approximately 30 min). The temperature was then increased to 300 °C until flameless self-combustion. The obtained powder was crushed in a mortar, transferred to a furnace, and annealed at 350 °C for 1 h and subsequently at a suitable higher temperature for a longer time (10 h). The synthesis was repeated several times for different annealing temperatures from 500 to 1000 °C. As illustrated in Fig. 1, the syntheses resulted in BTO powder with an additional barium carbonate $BaCO_3$ phase. For high annealing temperatures, the amount of $BaCO_3$ phase decreases, albeit another impurity phase (Ba_2TiO_4) starts appearing in the XRPD patterns (see Fig. 1b). The optimal annealing temperature (i.e. leading to the minimum amount of $BaCO_3$ and no other secondary phases) was found to be 650 °C when using glycine as a chelating agent, and 700 °C when using citric acid.

To obtain pure BTO powder, the samples annealed at the optimal temperatures were washed in acetic acid for some time and then dried at ~160 °C for some hours, to eliminate the $BaCO_3$ phase. The cationic Ba/Ti ratio was estimated from X-ray fluorescence to 1:1 within experimental error, suggesting the presence of negligible amounts of $BaCO_3$. The XRPD data of pure BTO powders obtained using both chelating agents and after washing are shown in Fig. 2. BTO adopts a tetragonal structure with space group *P4mm*. Lattice parameters estimated from the refinements of the XRPD data and average crystallite sizes estimated from Williamson-Hall plots [17] are presented in Table 1. Lattice parameters and c/a values are larger than that of bulk BTO, as observed earlier in several studies of size dependence effects in BTO nanostructures [18–20]. It has also been reported that the higher the calcination temperature, the larger the crystallite size and tetragonality of BTO powders [21].

Fig. 3 shows the temperature dependence of dielectric permittivity $\varepsilon_r(T)$ and loss-tangent Tanδ(T) recorded at various frequencies 100 Hz ≤ f ≤ 2 MHz for BTO. Two dielectric anomalies; a hump at 286 K and a broad peak at 392 K (as shown by arrows in Fig. 3a), are clearly noticed from the $\varepsilon_r(T)$ curve. These dielectric anomalies reflect the orthorhombic to tetragonal and tetragonal to cubic structural phase transitions of BTO across 286 and 392 K, respectively. The rhombohedral to orthorhombic transition across 190 K [7,22] is on the other hand not clearly visible in the present $\varepsilon_r(T)$ data nor Tanδ(T). The observed value of dielectric constant ($\varepsilon_r \sim 120$ at 300 K) is significantly smaller as compared to their bulk counterpart ($\varepsilon_r \sim 1000$ at 300 K for single crystal of BTO) [7]. The ferroelectric nature was further confirmed from the hysteresis and partially saturated polarization versus electric field loop (P-E loop) recorded at room temperature (inset of Fig. 3a).

Table 1
List of lattice parameters, c/*a* ratio for BTO obtained from Rietveld refinement for the various samples. The average crystallite size D and strain η estimated from Williamson-Hall plots is also indicated.

	a (Å)	**b** (Å)	**c** (Å)	**c/*a***	D (nm)	η × 10^{-4}
BTO nanoparticles						
BTO-Glycine 650 °C	4.0034 (2)	4.0034 (2)	4.0207 (3)	1.0043	44(2)	4.3 (4)
BTO-Citric acid 700 °C	4.0025 (2)	4.0025 (2)	4.0232 (2)	1.0051	43(2)	17.0 (3)
BTO-CFO nanocomposites						
BTO-CFO 95:05 Citric acid 700 °C	4.0061 (7)	4.0061 (7)	4.0219 (15)	1.0039	26(1)	8.7 (4)
BTO-CFO 90:10 Citric acid 700 °C	4.0073 (9)	4.0073 (9)	4.0225 (14)	1.0037	16(1)	18.0 (4)
BTO films						
BTO-Film-None	3.9945 (2)	3.99452 (2)	4.0398 (2)	1.0113	12(1)	11.0 (2)
BTO-Film-EG	3.9969 (2)	3.9969 (2)	4.0361 (3)	1.0098	11(1)	22.0 (2)
BTO-Film-EA	3.9986 (7)	3.9986 (7)	4.0221 (10)	1.0058	13(1)	19.0 (3)

4. BTO-CFO nanocomposites

The integration and coupling of the two phases of a nanocomposite and its morphology critically depend on the synthesis method [12]. While a suitable morphology may be obtained by using preformed particles as seeds for the second one [9], it was shown that a novel one-pot synthesis method, in which particles from both phases concurrently form, could be used to prepare strongly coupled phases [13]. Another advantage of that synthesis is that the formation of each phase participates to that of the other one in a symbiotic effect [13]. Bi-magnetic $LaFeO_3$-$CoFe_2O_4$ (LFO-CFO) nanocomposites were synthesized using the one-pot method. The detailed analysis of the structural and morphological properties of the nanocomposites revealed that the formation of the CFO phase and associated heat production promoted the growth of LFO, which in turn restricted the growth of CFO, yielding smaller particles [13]. The one-pot method has also successfully been used to synthesize ferroelectric-ferrimagnetic $PbZr_{0.52}Ti_{0.48}O_3$-$CoFe_2O_4$ nanocomposites [14], as well as hard-soft bi-magnetic hexaferrite-spinel oxide $SrFe_{12}O_{19}$-$CoFe_2O_4$ nanocomposites relevant to permanent magnets [23]. Nevertheless, applying this one-pot synthesis method to obtain BTO-CFO nanocomposite is non-trivial and requires careful optimization because of the concurrent formation of undesirable phases like $BaCO_3$ and Ba_2TiO_4 even during the synthesis of single-phase BTO (as mentioned in the previous section).

In the present case, two 0.1 M sols were first separately prepared at room temperature by dissolving the precursors in distilled water. The

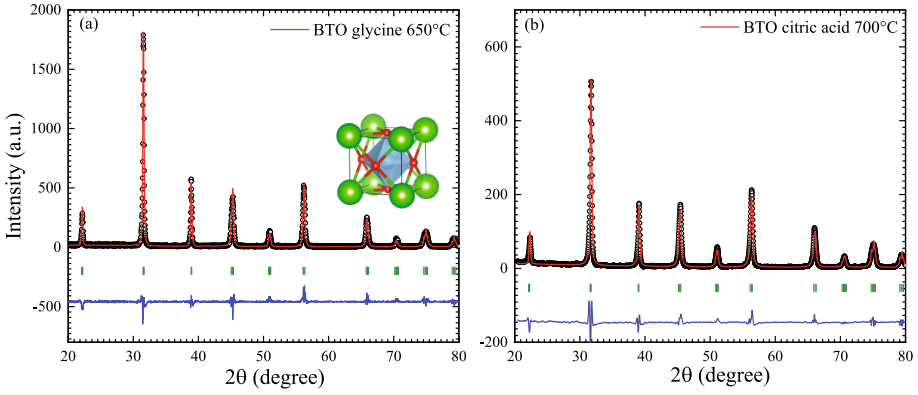

Fig. 2. XRPD patterns (black symbols) together with the Rietveld refined data (red line) of (a) BTO glycine 650 °C and (b) BTO citric acid 700 °C; the goodness of fit parameters R_p, R_{wp}, R_B and χ^2 are respectively (glycine) 22.7, 27.7, 19.8 and 1.94 and (citric acid) 16.4, 22.4, 16.7 and 1.80. The blue lines at the bottom represent difference between the measured and simulated patterns and vertical green lines shows the Bragg's peak position. Inset shows the polyhedral representation of the structural unit cell of BTO where Ba^{2+} (green), O^{2-} (red) and Ti^{4+} (blue) ions are located at the edge, face center and body center of the pseudo-cubic structure, respectively; drawn using VESTA [26].

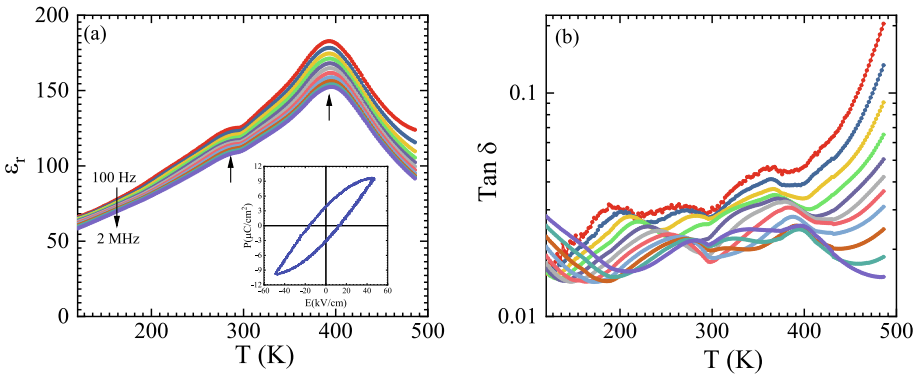

Fig. 3. Temperature dependence of (a) dielectric permittivity ε_r(T) and (b) loss-tangent Tanδ(T) recorded at various frequencies 100 Hz ≤ f ≤ 2 MHz for BTO citric acid 700 °C. Inset shows the Polarization versus electric field loop (P-E loop) recorded at room temperature and at a frequency of 500 Hz.

first one containing stoichiometric amounts of the precursors of CFO i.e., 0.00143 mol (0.4162 g) of Co-nitrate $Co(NO_3)_2{\cdot}6H_2O$ and 0.00286 mol (1.1554 g) of Fe-nitrate $Fe(NO_3)_3{\cdot}9H_2O$ (Sigma–Aldrich, ≥98% purity for both nitrates) dissolved in 14.3 ml of distilled water, and the other containing stoichiometric amounts of the precursors of BTO i.e., Ba-nitrate $Ba(NO_3)_2$ and Ti-isopropoxide $Ti[OCH(CH_3)_2]_4$; see the preparation of sol in previous section about BTO nanoparticles. The amount of chelating agent added (whether glycine or citric acid) is added such that number of moles of agent is equal to addition of number of moles of precursors. Suitable volumes of each of the two clear solutions were then mixed at room temperature and stirred for 20 min. This composite sol was then heated to 80 °C and stirred for 20 min. Next, the temperature was increased and maintained at ~150 °C, promoting the formation of a gel. The temperature was then increased to ~250 °C until flameless self-combustion. The obtained powder was crushed in a mortar, transferred to a furnace, and annealed in air at 350 °C for 1 h, followed by a final annealing at a higher temperature for 10 h. The different steps involved in the synthesis are illustrated in the flow chart presented in Fig. 4.

As for single-phase BTO nanoparticles, both glycine and citric acid were considered as chelating agents. In the case of glycine, the final annealing temperature was 650 °C while for citric acid it was 700 °C. Akin also to the BTO system, the obtained BTO-CFO composites need to be washed with acetic acid to remove secondary $BaCO_3$ phases. In addition, it was observed that increasing the CFO content led to an increase in the $BaCO_3$ content.

The XRPD patterns of BTO, CFO, and BTO-CFO synthesized using glycine are shown in the left panel of Fig. 5; results for nanocomposites with smaller CFO volume fractions obtained using citric acid are presented in the right panel. The XRPD curves for BTO-CFO composites prepared using glycine match that of a pure tetragonal phase with low intensity peaks related to CFO phase for the composite with higher CFO composition, i.e. BTO-CFO 80:20. Additional reflections not related to CFO may also be observed in the BTO-CFO 80:20 data, owing to the presence of some amounts of Ba_2TiO_4; this suggests that the optimum final annealing temperature might be slightly different than 650 °C in BTO-CFO with significant amounts of CFO. No such phase is observed in the BTO-CFO composites with lower CFO contents prepared using the citric acid route presented in the right panel of Fig. 5. The XRPD data for those samples were refined, without considering CFO as a secondary phase owing to its low content. The obtained lattice parameters and average crystallite sizes are presented in Table 1.

Fig. 6 shows the field dependence of magnetization of the BTO-CFO nanocomposites recorded at T = 300 K (left) and T = 5 K (right). BTO is expected to show diamagnetism. However, the two nanocomposites have magnetic properties reminiscent of the ferrimagnetic behavior of CFO, up to room-temperature (left panel). The coercivity H_c of the nanocomposites was found to be 0.51 T and 0.77 T at T = 5 K, and 0.13 T and 0.14 T at T = 300 K for BTO-CFO 90:10 and 80:20, respectively. The

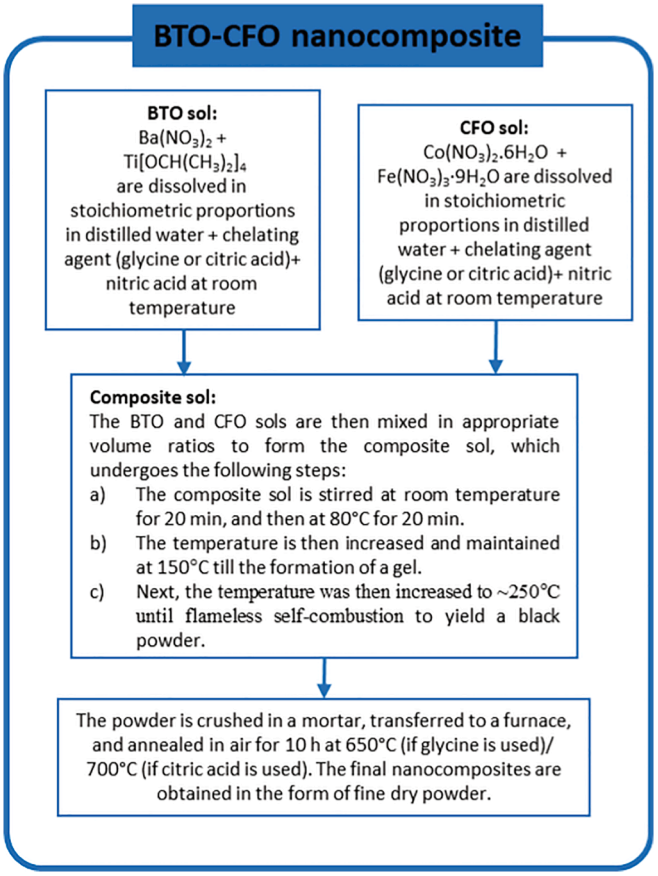

Fig. 4. Flow chart describing the different steps of the synthesis of BTO-CFO nanocomposites.

magnetic field dependence of the remanent magnetization was recorded at low temperatures using the DCD protocol [24,25], i.e. after saturating the system in a field of −5 T, and recording the remanent magnetization for a series of increasing reverse (positive) fields H (see Fig. 7a). The so-called remanence coercivity H_{cr} ($M_{DCD}(H_{cr}) = 0$) is around 1 T in both cases, suggesting a similar anisotropy for both materials. The ratio H_c/H_{cr} increases from BTO:CFO 90:10 to BTO:CFO 80:20, suggesting that the increase of coercivity with the increase of CFO content may reflect differences in particle size distribution [12]. The derivative of M_{DCD} curve with respect to the reverse field yields the irreversible susceptibility χ_{irr} which reflects the distribution of particle switching field distributions. As seen in Fig. 7b, the $\chi_{irr}(H)$ curves of both composites show relatively sharp peaks, suggesting a relatively homogeneous process of

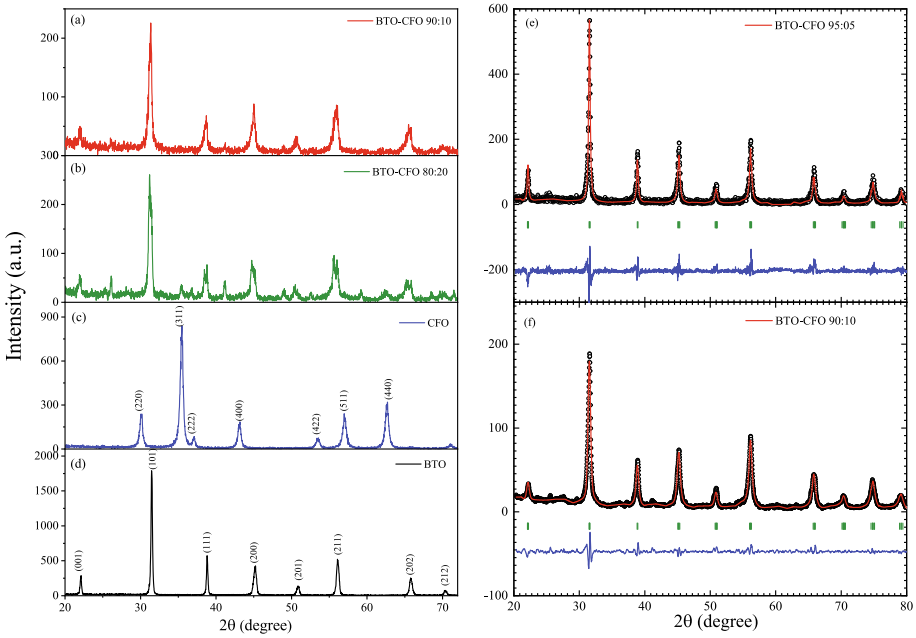

Fig. 5. XRPD patterns for (a) BTO-CFO 90:10, (b) BTO-CFO 80:20 (c) CFO and (d) BTO with glycine route; (e) and (f) shows the XRPD patterns and Rietveld refinements for BTO-CFO 95:05 and BTO-CFO 90:10 using citric acid route. The goodness of fit parameters R_p, R_{wp}, R_B and χ^2 are respectively (95:05) 21.8, 18.3, 11.38 and 2.6 and (90:10) 24.9, 23.07, 10.45 and 5.15.

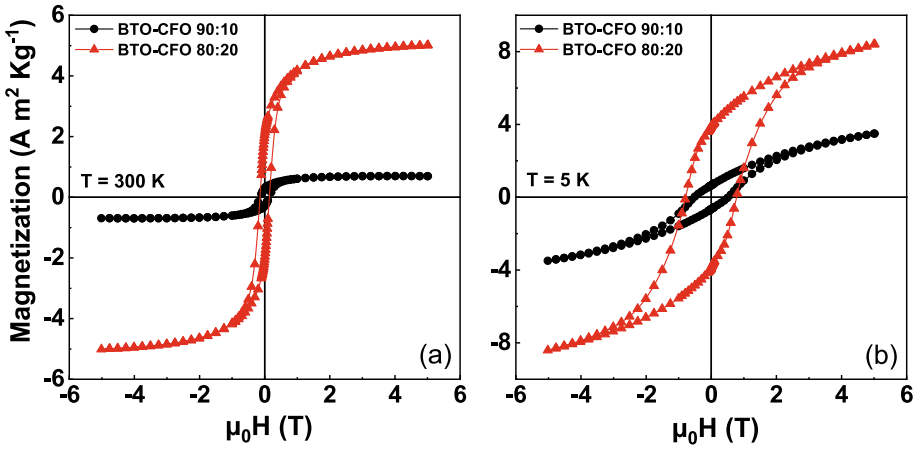

Fig. 6. Compared isothermal magnetization curves of BTO-CFO composite powders (90:10 and 80:20) at (a) T = 300 K and (b) T = 5 K respectively (650 °C glycine samples).

magnetization reversal, and again a similar magnetic anisotropy for both nanocomposites.

The ε_r(T) and Tanδ(T) curves recorded at various frequencies 100 Hz $\leq$ f $\leq$ 2 MHz for BTO-CFO 95:05 nanocomposite are shown in Fig. 8a and 8b, respectively. The incorporation of CFO inside the BTO nanoparticles decreases the dielectric constant ($\varepsilon_r \sim 12$ at 300 K) as well as lowers the transition temperatures (224 K and 350 K at 73 kHz) as compared to BTO nanoparticles. Moreover, the dielectric permittivity shows strong frequency dispersion, which might be associated with the disruption of long-range ferroelectric ordering by the addition of non-ferroelectric CFO phase inside BTO. Nevertheless, The P-E loop recorded at room temperature (inset of Fig. 8a) displays similar hysteresis loops as single-phase BTO (inset of Fig. 3a). For BTO:CFO 90:10 nanocomposite, the P-E loops are shifted from the origin (not shown in the manuscript), possibly due to the leakage currents and non-linear dielectric effects associated with the conductive CFO phase.

5. Spin-coated thin films: Preliminary results

For many applications, it is necessary to use thin films and/or micro- and nanostructures obtained after patterning thin films [4]. However, the solutions obtained above before combustion could not be spin coated onto substrates owing to the employed chelating agents, which restrict the maximum dimensions of the final materials.

Several trials were conducted using different precursors and agents, at first with nanoscale BTO. A suitable recipe was obtained to prepare phase pure solutions, which could be successfully spin coated onto substrates. A 0.3 M solution was prepared as follows: 0.766 g Ba-acetate $Ba(C_2H_3O_2)_2$ (Sigma–Aldrich, ≥99% purity) was dissolved in 5 ml glacial acetic acid and stirred at 60 °C until the Ba-acetate dissolved completely. The solution was then cooled to room temperature. Then 1.02 ml of Ti-butoxide Ti($OCH_2CH_2CH_2CH_3$)$_4$ (Sigma–Aldrich, ≥97% purity) was added to the solution, as well as 0.335 ml of ethelyne glycol (EG) as chelating agent to form stock solution. Next, the solution was diluted with equal volume of 2-methoxyethanol (5 ml) and stirred for

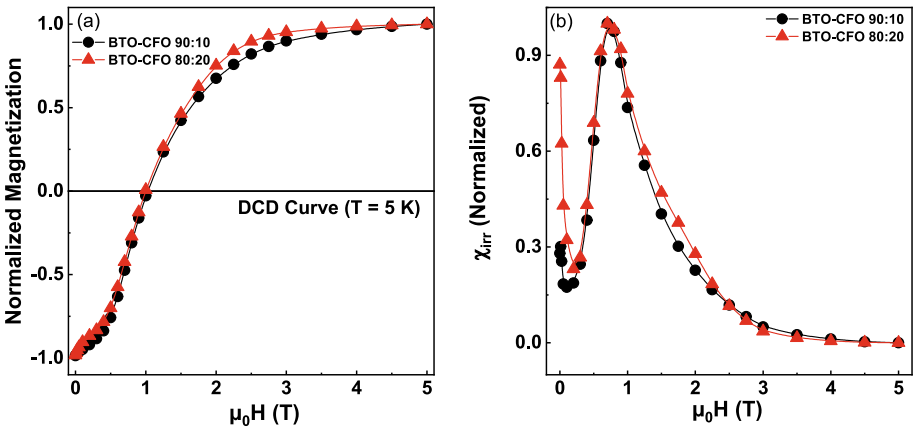

Fig. 7. Normalized (a) direct current demagnetization (DCD) curves and (b) switching field distributions of BTO-CFO composite powders (90:10 and 80:20; 650 °C glycine samples).

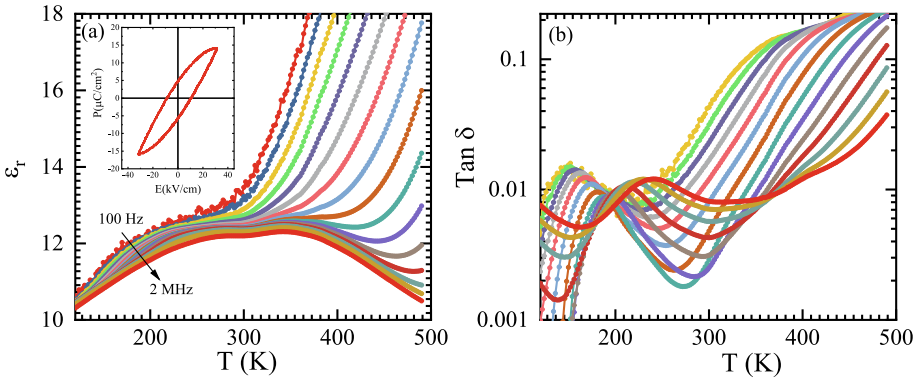

Fig. 8. Temperature dependence of (a) dielectric permittivity ε_r(T) and (b) loss-tangent Tanδ(T) recorded at various frequencies 100 Hz ≤ f ≤ 2 MHz for BTO-CFO 95:05 (citric acid 700 °C samples). Inset shows the Polarization versus electric field loop (P-E loop) recorded at room temperature and at a frequency of 500 Hz.

one hour at room temperature to form a homogeneous mixture. Satisfactory results were also obtained using ethanolamine (EA) instead of ethylene glycol as chelating agent, as well as without chelating agent. The flow chart in Fig. 9 illustrates the different synthesis steps.

The obtained solutions were spin coated on cleaned Si, baked at 200 °C for 5 min, and annealed at 650 °C for 1 h, forming thin films. In Fig. 10, we show the XRPD patterns of pure BTO films obtained using EG and EA as chelating agent, and without chelating agent. The three XRPD patterns show pure tetragonal BTO phase; yet with some reflections with small intensities related to the substrate. Lattice parameters and average crystallite sizes are presented in Table 1. The thickness of the films was estimated to about 50 nm by using the profilometer. Substrates were found to be not conductive enough to permit dielectric measurements.

The one-pot synthesis method has also been employed to obtain thin films of $LaFeO_3$-$CoFe_2O_4$ [13]. The synthesis of films of multiferroic BTO-CFO was hence attempted. Although we could not obtain phase pure films, we present the results obtained by combining the know-how gathered during the syntheses of BTO thin films and BTO-CFO nanocomposites, as the results suggest that phase pure films could be obtained after further optimization of the synthesis and heat treatments (e.g. quenching, aging the solution).

As for the nanocomposites, two solutions were prepared separately and mixed. The BTO solution was prepared as mentioned in the previous section using EA as a chelating agent. For the CFO solution, cobalt acetate tetrahydrate and iron nitrate nonahydrate were used as precursors; EA was used as chelating agent and 2-methoxyethanol [14]. The two solutions were then mixed with the required proportions to match the composition to be prepared. The composite solution is mixed for about one hour to insure homogeneity. Although 650 °C was found to be the

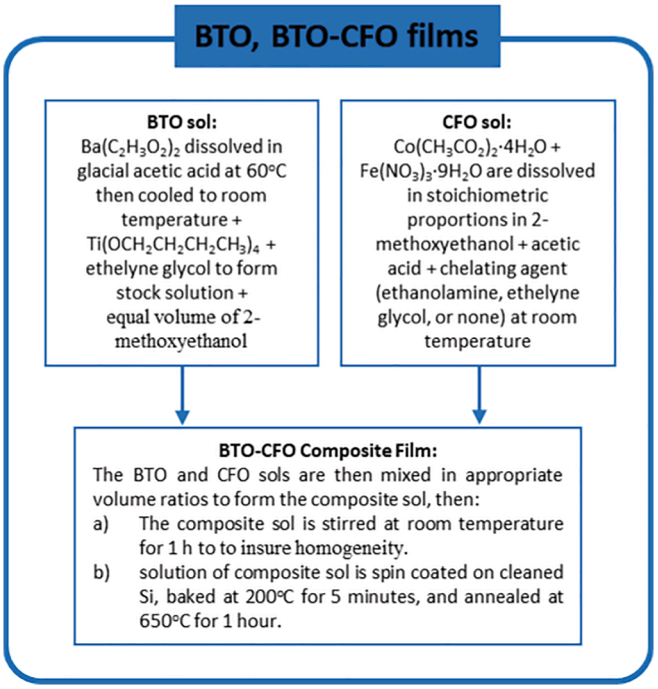

Fig. 9. Flow chart describing the different steps of the synthesis of BTO and BTO-CFO films. For BTO films, the BTO sol is spin coated on the Si substrates, and baked and annealed in the same conditions as indicated.

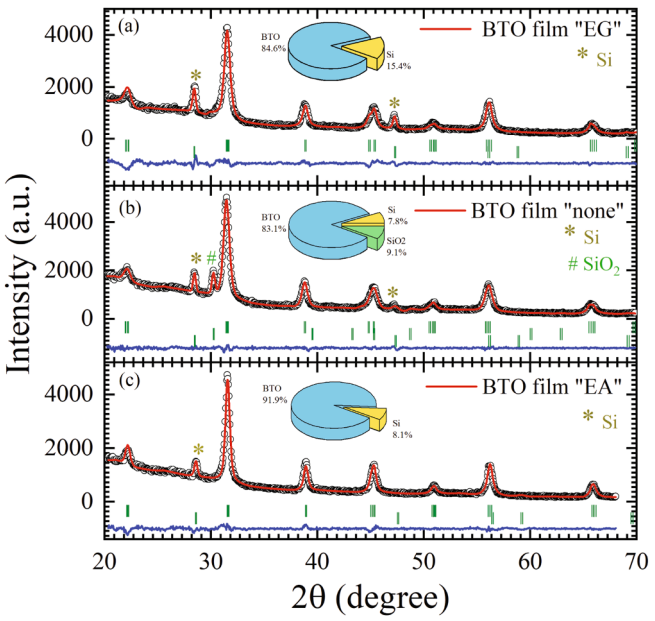

Fig. 10. XRPD patterns and Rietveld refinements of BTO films prepared using (a,c) with chelating agent (a: ethylene glycol, "EG" and c: ethanolamine "EA"), and (b) without chelating agent (labeled "none"). The goodness of fit parameters R_p, R_{wp}, R_B and χ^2 are respectively (EG) 20.4, 17.8, 11.0 and 2.62; (EA) 18.8, 15.6, 11.04 and 1.99; (none) 14.3, 12.3, 10.43 and 1.40. The pie-charts shown in the insets represent the quantitative phase analysis performed using the RIR method.

best annealing temperature for BTO films, a higher temperature was necessary in the case of the composite films. Tetragonal BTO phase is clearly observed in a BTO-CFO 90:10 film annealed at 700 °C (see Fig. 11), however, a secondary phase is present.

6. Conclusion

In summary, the optimization of the chemical synthesis of BTO and BTO-CFO nanostructures was presented. In the case of the BTO-CFO nanocomposites, a novel composite sol-based synthesis technique for complex oxide nanocomposites was employed. We have identified the suitable solvents, chelating agents, temperatures, and other synthesis conditions permitting the synthesis of nanoscale BTO and BTO-CFO, as confirmed from XRPD studies. Thin films of BTO could also been obtained, while the conditions for phase-pure BTO-CFO needs to be refined further. The reported magnetic and electric properties suggest that multiferroic bi-phasic BTO-CFO thin films may be fabricated. The reported magnetic and electric properties suggest that multiferroic bi-phasic BTO-CFO thin films may be fabricated. Once the optimum synthesis conditions of the nanostructures in "bulk" and film forms are fully established, it will be very relevant to investigate the structural, morphological, and interfacial properties of the systems in more detail using high-resolution transmission electron microscopy.

Author contribution statement

F.S. performed the synthesis, chemical analysis and collected and analyzed the diffraction data. G.N. participated to the synthesis and characterization of thin films. T.S. developed the synthesis method. D.C. J. was responsible for dielectric data collection and analysis, as well as structural refinements. F.S. and T.S. performed magnetic measurements. T.S. D.P. and R.M. supervised the study. All authors contributed to the writing of the manuscript.

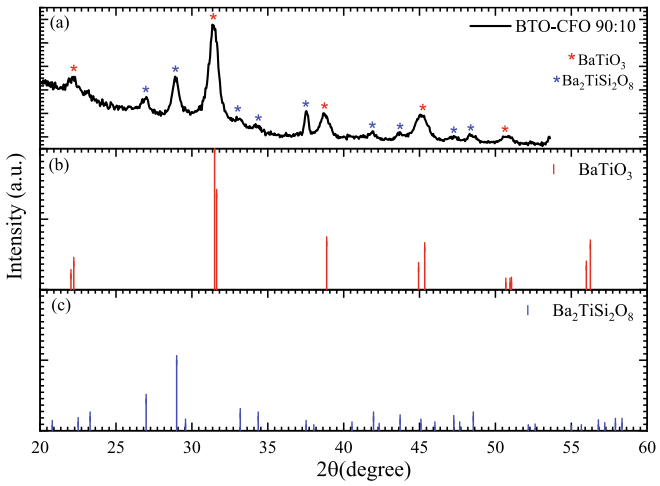

Fig. 11. (a) XRPD pattern for BTO-CFO 90:10 composite film annealed at 700 °C for 1 h. (b) and (c) shows the standard Bragg's peak reflections for $BaTiO_3$ and $Ba_2TiSi_2O_8$, respectively.

Declaration of Competing Interest

The authors declare that they have no known competing financial interests or personal relationships that could have appeared to influence the work reported in this paper.

Acknowledgements

We thank Carl Tryggers Stiftelse för Vetenskaplig Forskning (grant number KF 17:18), Stiftelsen Olle Engkvist Byggmästare (grant numbers: 184-546 and 188-0179), Swedish Research Council (including VR starting grant number: 2017-05030), and the Royal Physiographic Society of Lund (the Märta and Eric Holmberg Endowment) for financial support.

References

[1] N.A. Spaldin, R. Ramesh, Advances in magnetoelectric multiferroics, Nat. Mater. 18 (2019) 203.
[2] S. Manipatruni, D.E. Nikonov, C.-C. Lin, T.A. Gosavi, H. Liu, B. Prasad, Y.-L. Huang, E. Bonturim, R. Ramesh, I.A. Young, Scalable energy-efficient magnetoelectric spin–orbit logic, Nature 565 (2019) 35.
[3] H. Zheng, J. Wang, S.E. Lofland, Z. Ma, L. Mohaddes-Ardabili, T. Zhao, L. Salamanca-Riba, S.R. Shinde, S.B. Ogale, F. Bai, D. Viehland, Y. Jia, D.G. Schlom, M. Wuttig, A. Roytburd, R. Ramesh, Multiferroic $BaTiO_3$-$CoFe_2O_4$ nanostructures, Science 303 (2004) 661.
[4] D. Erdem, N.S. Bingham, F.J. Heiligtag, N. Pilet, P. Warnicke, C.A.F. Vaz, Y. Shi, M. Buzzi, J.L.M. Rupp, L.J. Heyderman, M. Niederberger, Nanoparticle-based magnetoelectric $BaTiO_3$–$CoFe_2O_4$ thin film heterostructures for voltage control of magnetism, ACS Nano 10 (2016) 9840.
[5] L.V. Leonel, A. Righi, W.N. Mussel, J.B. Silva, N.D.S. Mohallem, Structural characterization of barium titanate cobalt ferrite composite powders, Ceram. Int. 37 (2011) 1259.
[6] I. Fina, N. Dix, L. Fàbrega, F. Sánchez, J. Fontcuberta, Magnetocapacitance in $BaTiO_3$-$CoFe_2O_4$ nanocomposites, Thin Solid Films 518 (2010) 4634.
[7] Y. Akishige, T. Nakanishi, N. Mori, Dielectric dispersion in $BaTiO_3$ single crystal at low temperatures, Ferroelectrics 217 (1998) 217.
[8] V.A.M. Brabers, progress in spinel ferrite research, in: Handbook of Magnetic Materials, North-Holland/Elsevier, Amsterdam, 1995, p. 212.
[9] G. Muscas, P. Anil Kumar, G. Barucca, G. Concas, G. Varvaro, R. Mathieu, D. Peddis, Designing new ferrite/manganite nanocomposites, Nanoscale 8 (2016) 2081.
[10] B. Balamurugan, D.J. Sellmyer, G.C. Hadjipanayis, R. Skomski, Prospects for nanoparticle-based permanent magnets, Scr. Mater. 67 (2012) 542–547.
[11] T. Sarkar, G. Muscas, G. Barucca, F. Locardi, G. Varvaro, D. Peddis, R. Mathieu, Tunable single-phase magnetic behavior in chemically synthesized $AFeO_3$–MFe_2O_4 (A = Bi or La, M = Co or Ni) nanocomposites, Nanoscale 10 (2018) 22990.
[12] F. Sayed, G. Muscas, S. Jovanovic, G. Barucca, F. Locardi, G. Varvaro, G.D. Peddis, R. Mathieu, T. Sarkar, Controlling magnetic coupling in bi-magnetic nanocomposites, Nanoscale 11 (2019) 14256.
[13] F. Sayed, G. Kotnana, G. Muscas, F. Locardi, A. Comite, G. Varvaro, D. Peddis, G. Barucca, R. Mathieu, T. Sarkar, Symbiotic, low-temperature, and scalable

synthesis of bi-magnetic complex oxide nanocomposites, Nanoscale Adv. 2 (2020) 851.
[14] G. Kotnana, F. Sayed, D.C. Joshi, G. Barucca, D. Peddis, R. Mathieu, T. Sarkar, Novel mixed precursor approach to prepare multiferroic nanocomposites with enhanced interfacial coupling, J. Magn. Magn. Mater. 511 (2020), 166792.
[15] F. Sayed, G. Kotnana, G. Barucca, G. Muscas, D. Peddis, R. Mathieu, T. Sarkar, $LaFeO_3$-$CoFe_2O_4$ bi-magnetic composite thin films prepared using an all-in-one synthesis technique, J. Magn. Magn. Mater. 503 (2020), 166622.
[16] J. Rodriguez-Carvajal, Recent advances in magnetic structure determination by neutron powder diffraction, Phys. B 192 (1993) 55.
[17] G.K. Williamson, W.H. Hall, X-ray line broadening from filed aluminium and wolfram, Acta Metall. 1 (1953) 22.
[18] J. Hong, D. Fang, Size-dependent ferroelectric behaviors of $BaTiO_3$ nanowires, Appl. Phys. Lett. 92 (2008), 012906.
[19] O.G. Grendal, A.B. Blichfeld, S.L. Skjærvø, W.V. Beek, S.M. Selbach, T. Grande, M.-A. Einarsrudet, Facile low temperature hydrothermal synthesis of $BaTiO_3$ nanoparticles studied by in situ X-ray diffraction, Crystals 8 (2018) 253.
[20] D.-H. Yoon, Tetragonality of barium titanate powder for a ceramic capacitor application, J. Ceram. Proces. Res. 7 (2006) 343.
[21] N.M. Zali, C.S. Mahmood, S.M. Mohamad, C.T. Foo, J.A. Murshidi, X-ray diffraction study of crystalline barium titanate ceramics, AIP Conf. Proc. 1584 (2014) 160.
[22] M. Acosta, N. Novak, V. Rojas, S. Patel, R. Vaish, J. Koruza, G.A. Rossetti Jr, J. Rödel, $BaTiO_3$-based piezoelectrics: Fundamentals, current status, and perspectives, Appl. Phys. Rev. 4 (2017) 41305.
[23] P. Maltoni, T. Sarkar, G. Varvaro, G. Barucca, S.A. Ivanov, D. Peddis, R. Mathieu, Towards bi-magnetic nanocomposites as permanent magnets through the optimization of the synthesis and magnetic properties of $SrFe_{12}O_{19}$ nanocrystallites, J. Phys. D Appl. Phys. 54 (2021), 124004.
[24] O. Henkel, Remanenzverhalten und Wechselwirkungen in hartmagnetischen Teilchenkollektiven, Phys. Status Solid. 7 (1964) 919.
[25] E.P. Wohlfarth, Relations between Different Modes of Acquisition of the Remanent Magnetization of Ferromagnetic Particles, J. Appl. Phys. 29 (1958) 595; P.E. Kelly, K. O'Grady, P.I. Mayo, R.W. Chantrell, Switching mechanisms in cobalt-phosphorus thin films, IEEE Trans. Magn. 25 (1989) 3881.
[26] K. Momma, F. Izumi, VESTA 3 for three-dimensional visualization of crystal, volumetric and morphology data, J. Appl. Crystallogr. 44 (2011) 1272.